Cobalt Doped Bioactive Glasses: Sinterability, Crystallization Trend, and Biodegradation Assessment of Relevant Glass-Ceramic Scaffolds

Ahad Saeidi[1], Sara Banijamali[1],*, Mojgan Heydari[2]

* *banijamali@merc.ac.ir & banijamalis@yahoo.com*

[1] Department of Ceramic, Materials and Energy Research Center, Karaj, Iran
[2] Department of Nano Technology and Advanced Materials, Materials and Energy Research Center, Karaj, Iran

Abstract: This study explores the fabrication, structural analysis, and cytocompatibility of cobalt-doped bioactive glass scaffolds for potential applications in bone tissue engineering. A specific glass composition modified from Hench's original formulation was melted, quenched, and ground to an average particle size of 10 μm. The resulting amorphous powder underwent controlled sintering to form green bodies and was extensively characterized using simultaneous differential thermal analysis (DTA), Raman spectroscopy, and Fourier Transform Infrared analysis (FTIR). After mixing with a resin and a dispersant, the composite was used in digital light processing (DLP) 3D printing to construct scaffolds with interconnected macropores. Thermal post-treatment of 3D printed scaffolds, including debinding (Removing the binder used for shaping) and sintering, was optimized based on thermogravimetric analysis (TG) and the microstructure was examined using FE-SEM and XRD. In vitro, bioactivity was assessed by immersion in simulated body fluid (SBF), while cytocompatibility with MC3T3 cells was evaluated through SEM following a series of ethanol dehydration. The study validates the fabrication of bioactive glass scaffolds with recognized structural and morphological properties, establishing the effects of cobalt doping on glass behavior and its implications for tissue engineering scaffolds. Results show that low cobalt levels modify the glass network and reduce its Tg to 529°C, while higher concentrations enhance the structure at the point of its connectivity. XRD results show all prepared glasses are amorphous, and DTA suggests a concentration-dependent Tg relationship. Spectroscopy indicates potential Si-O-Co bonding and its effects on SiO₂ polymerization. Cobalt's nucleating role promotes crystalline phases, enhancing bioactivity seen in rapid CHA layer formation in SBF, and advancing the prospects for bone tissue engineering materials.

Keywords: Tissue engineering, Bioactive glass-ceramic, Scaffold, Glass structure.

1. INTRODUCTION

Tissue engineering utilizes a scaffold made of a biocompatible natural or synthetic material to promote tissue regeneration. The scaffold serves as a substrate that supports the activity of bone cells and facilitates molecular and mechanical signalling systems to optimize tissue regeneration [1]. Biomaterials used in tissue engineering can be classified as bioinert, bioresorbable, or bioactive. Bioinert materials, such as alumina or titania, do not cause toxic responses but may induce fibrous tissue formation, preventing tissue bonding [2]. Bioresorbable materials, like tricalcium phosphate or biodegradable polymers, dissolve in the physiological environment and can be used as temporary scaffolds [3]. Bioactive glass-ceramic scaffolds have also been developed, which mimic cancellous bone structure and exhibit appropriate mechanical properties and bioactivity to support new bone formation [4]. Bioactive glasses have been extensively studied for their potential applications in tissue

engineering and wound healing [5]. One specific type of bioactive glass is the 45S5 scaffold, which has been widely used in various tissue engineering applications, particularly for bone repair and regeneration [6]. The 45S5 scaffold is composed of a sodium-calcium-silicate glass that can dissolve incongruently, yielding hydrous silica and providing nucleation sites for hydroxyapatite precipitation [7]. This scaffold has shown promising results in stimulating bone repair and osseointegration when used in periodontal repair and metallic implant coatings. Additionally, the incorporation of therapeutic ions within the composition of bioactive glasses, including the 45S5 scaffold, has been explored to enhance their functionality and promote tissue regeneration [8].

The addition of cobalt to bioactive 45S5 glasses has been shown to have various effects on their properties. The presence of Co^{2+} ions in phosphate glasses leads to the formation of new blood vessels, promoting angiogenesis (<10% mol) [9]. However, prolonged exposure to cobalt-

containing glasses can reduce cell proliferation, metabolic activity, and chondrogenic differentiation, making it necessary to carefully consider its use in cartilage repair applications [10]. On the other hand, cobalt incorporation in the sol-gel bioactive glasses has been found to stimulate the formation of blood vessels and the expression of angiogenesis-related genes, making it a promising strategy for tissue engineering applications [11]. Cobalt-doped bioactive glasses have also shown potential for improving angiogenesis in regenerative medicine approaches, although concerns about possible toxic effects on living cells and tissues remain [12]. Overall, the addition of cobalt to bioactive glasses can have both beneficial and detrimental effects on their properties, depending on the specific application and concentration of cobalt ions [11].

In this work, we present a comprehensive study on the effect of cobalt-doped modified 45S5 bioactive glasses within the SiO_2-Na_2O-K_2O-MgO-CaO-P_2O_5-B_2O_3 system, examining a spectrum of compositions with varying CoO content. The physicochemical characterization of these (Bioactive Glass/ (0-5%) Co) BG-Co, through techniques such as X-ray diffraction, Fourier-transform infrared spectroscopy, and Raman, allowed us to unravel the influence of Co ions on the BG structural network. This article elucidates the dual role that Co ions play in bioactivity as a function of their concentration. Additionally, we investigate the dissolution behavior of BG-xCo and their interactivity with biological fluids, defining the prospects of their usage. By providing a deepened understanding of the structure-property interaction, we lay the groundwork for the potential clinical translation of cobalt-doped bioactive glasses, designed to meet the multifaceted demands of bone tissue engineering.

2. EXPERIMENTAL PROCEDURES

2.1. Glass Preparation

High-purity Silica (SiO_2), phosphorus oxide (P_2O_5), calcium carbonate ($CaCO_3$), sodium carbonate (Na_2CO_3), potassium carbonate (K_2CO_3), magnesium carbonate hydroxide, and boric acid (H_3BO_3), powders were weighed and mixed to obtain Co-doped bioactive glass (SiO_2 48, K_2O 20, CaO 18, Na_2O 5, P_2O_5 4, B_2O_3 3, MgO 2, XCoO (x= 0, 1, 3, 5) (Table 1). The bioactive glass used in this research is the original composition developed by Hench et al. in 1971, which was later modified based on research by Zannoto's group. The precursor powders of the oxides were melted in a zirconia crucible for 1 hour at 1350°C. Subsequently, the molten material was quenched in water and ground into a fine powder with an average particle size of 10 μm. The rapid quenching process effectively preserved the material in a completely amorphous state, as confirmed by X-ray diffraction analysis (Fig 4).

2.2. Structure and Thermal Properties

The changes in physical and chemical characteristics of the glass powder were observed using simultaneous differential thermal analysis (DTA) with the Polymer Laboratories 1640 instrument. In the DTA process, 20 mg of powder was heated in an atmosphere composed of 20% N_2 and 80% O_2 at a rate of 10°C per minute, reaching temperatures up to 1000°C.

To investigate the cobalt effect on the structure of bioactive glass, two types of analyses were conducted: Raman Spectroscopy (Teksan with a 532 nm wavelength) and Fourier Transform Infrared analysis (FTIR, Bruker Tensor 27).

To identify the nature of the chemical bonds between atoms, FTIR analyses were conducted. The samples, composed of compacted glass powder and potassium bromide, formed small pellets with a diameter of 0.5 cm through the pressing process.

2.3. Characterization of Sintering Behavior

Several thermal treatments were carried out on the dried compacted glass in the range of 600–850°C, each lasting for 60 minutes with a heating rate of 5°C/min.

Table 1. The nominal composition of the bioactive glasses

Sample Code	SiO₂	Na₂O	K₂O	MgO	CaO	P₂O₅	B₂O₃	Co
BG-0Co	48	5	20	2	18	4	3	0
BG-1Co	48	5	20	2	18	4	3	1
BG-3Co	48	5	20	2	18	4	3	3
BG-5Co	48	5	20	2	18	4	3	5

To create green bodies, the glass powder (<45 µm) was homogeneously mixed with 0.5 wt % PVA. These mixtures were then poured into stainless-steel cylindrical dies. Subsequently, the mixtures were pressed under a pressure of 426.85 Kg/cm^2, forming green bodies measuring 12 mm in diameter and 3 mm in height.

The sintering behaviour of the glass bodies was evaluated through three methods: water absorption, bulk density, and linear shrinkage of samples.

2.4. Scaffold Fabrication

2.4.1. 3D printing of scaffolds

In this part of the research, a melt-derived bioactive glass powder with an average particle size ranging from 10 to 20 µm was used. The fabrication of bioactive glass scaffolds was conducted using the DLP method.

For this purpose, a composition containing 60 wt% bioactive glass, 40 wt% commercially available resin (Anycubic Colored UV Resin), and 2 wt% oleic acid (Based on glass powder) as a dispersant was used. This composition featured high flowability, which is crucial for powder-based printing.

The powder was homogenized in a laboratory blender for 30 minutes at a speed of 350 RPM. Cylindrical samples, incorporating interconnected macropores as illustrated in Fig 1, were designed using CAD software, specifically SolidWorks 2016 SP 5.0. Subsequently, the composite Resin was 3D printed using a commercially available 3D printer, the Anycubic Photon Mono X 6K (HONGKONG ANYCUBIC TECHNOLOGY) (Fig 2(a)), and its schematic structure is illustrated in Fig 2 (b).

Fig 2 depicts the printing principle employed in the DLP method. During the initial printing stage, the separation between the printing platform or printing part and the upper surface of the transparent membrane indicates the thickness of a single cured layer, as illustrated in Fig 2 the light source projects a sliced image of the model onto the designated layer and induces the solidification of the paste.

Properties	Scaffold
Diameter (d)	15 mm
Height (h)	15 mm
Pore diameter	2 mm

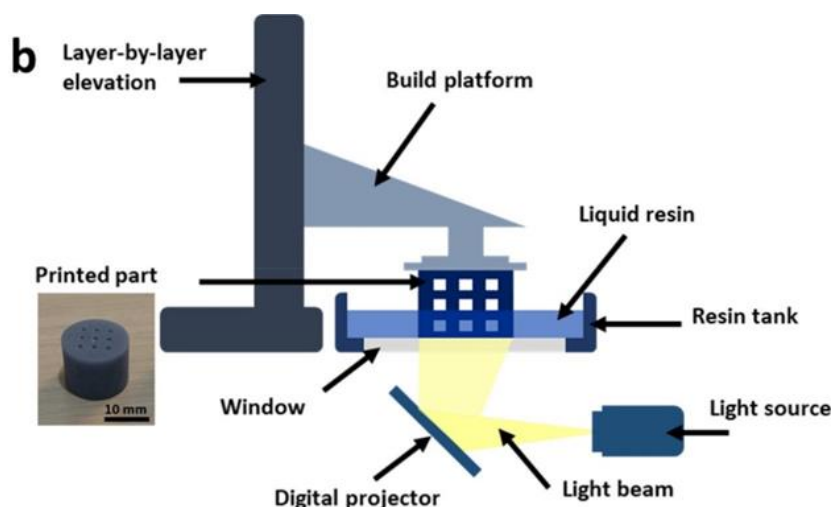**Fig. 1.** CAD Design and geometrical data of Bioactive glass scaffolds.

Fig. 2. a) 3D printer used in this project, b) DLP Process schematic

3

After the complete solidification of the paste, the build platform is elevated, creating an opening in the rotating trough caused by the limited fluidity of the high-viscosity resin. Through the repetition of the processes, the part undergoes layer-by-layer stacking until the printing is complete.

Considering that the sintering behavior of the samples was close to each other and we wanted to investigate the maximum effect of cobalt, the 5% sample was used as a representative for further investigation.

2.4.2. Thermal post-treatment of 3D printed scaffolds

Thermogravimetric analysis (TG) was conducted using a TG analyzer (NETZSCH STA 449F3, Germany). In this assessment, 4.725 mg of the printed solid sample underwent heating from 25°C to 1000°C. The chosen maximum temperature of 1000°C aligns with the debinding process (remove binding agents (resin) in the part before the sintering process), where weight loss occurs. The heating rate was 5°C/min, performed in an alumina crucible, and under an air atmosphere. Various parameters, including the stages of weight loss, the onset temperature of thermal decomposition, and maximum and final thermal decomposition temperatures were determined. The thermal post-treatment of 3D printed scaffolds was designed based on the results of TG analysis and the optimum sintering temperature determined in the previous section. Thermal post-treatment was conducted to eliminate the polymeric phase from the samples and to enhance the solidity and density of the 3D-printed scaffolds. The polymeric phase was eliminated through pyrolysis from the scaffolds, a process known as debinding. This involved subjecting the scaffolds to heat treatment in a debinding furnace at 200°C for 30 minutes, followed by a subsequent treatment at 550°C for 90 minutes, as illustrated in Fig 3. As a final step, the debond green components underwent an additional sintering process at 650°C in a controlled atmosphere, lasting for 1 hour, as depicted in Fig 3.

2.4.3. Characterization of 3Dprinted and sintered bioactive glass scaffolds

The shrinkage of the scaffolds after 3D printing and after sintering was determined. The microstructure and elemental composition of the printed and sintered bioactive glass scaffolds were investigated using a TESCAN-MIRA3 model FE-SEM. Structural composition analysis was conducted using X-ray diffraction (XRD).
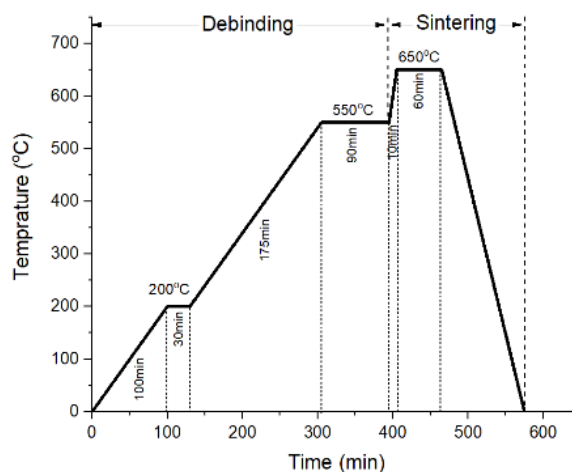

Fig. 3. Heat treatment schedule for debinding and sintering of 3D-printed bioactive glass scaffolds

2.5. Bioactivity Assessments

2.5.1. Evaluation of in vitro bioactivity

In recent years, there has been an observed formation of a calcium phosphate-rich layer on the surface of bioactive glasses when immersed in synthetic solutions designed to simulate physiological plasma. In 1990, Kokubo *et al.* [13]. introduced the Tris-buffered simulated body fluid (SBF) No. 9 for the in vitro investigation of bioactive glasses. This solution equals the ion concentration of human blood plasma. SBF can be used to study the in vitro bioactivity of a wider variety of materials due to its inclusion of calcium and phosphorous ions. As a result, in vitro studies in simulated body fluid (SBF) have gained popularity as initial assessments for potential implant materials. The in vitro bioactivity assessment involved immersing the bioactive glass scaffolds in 40 mL of a cell-free simulated body fluid, as suggested by Kokubo et al. (13), within sterile polyethylene containers at 37°C. The composition and concentration of the SBF solution closely resemble the inorganic components found in human plasma. This solution was created by dissolving reagent-grade NaCl, KCl, K_2HPO_4, $MgCl_2$, $CaCl_2$, and Na_2SO_4 in distilled water. pH was adjusted to 7.4 using hydrochloric acid at 37°C. The soaking durations comprised intervals of 4, 7, 14, and 21 days. The pH was systematically monitored at regular intervals during the immersion process using a

Mettler-Toledo pH meter (TMP-85). Following the soaking process, the samples were washed with acetone and air-dried at room temperature. Subsequently, the dried samples underwent examination using XRD, FTIR, and SEM.

2.5.2. Direct Cytocompatibility Test

The experiment began by cutting the scaffolds into pieces with a cross-sectional area of less than 1 cm² and a thickness of less than 5 millimetres, followed by multiple disinfection cycles using ultraviolet rays. To ensure complete disinfection, the scaffolds were immersed in 70% alcohol for 4 hours. Subsequently, the alcohol was removed, and the scaffolds were washed with PBS solution.

The scaffolds were placed inside wells of a plate, and a glucose culture medium was added to the wells. To ensure the absence of contamination in the scaffolds, the plate was kept in the incubator for 24 hours. Then, 20,000 osteoblastic cells (63-MG) were added to each well, and the plate was placed in the incubator at 37°C with 80% humidity and 5% CO_2. Next, tetrazolium salt yellow (3-(4,5-dimethylthiazol-2-yl)- 2,5-diphenyltetrazolium bromide or MTT) was prepared at a concentration of 5 mg/ml. On days 3 and 7, the culture medium was removed from the wells, and MTT ink, at a weight percentage of 10%, was added to the fresh culture medium. Then, the plate was incubated for three hours at 37°C to form formazan crystals, indicating the activity of mitochondrial enzymes in live cells. The formation of these crystals indicates the activity of respiratory chain enzymes and serves as a criterion for cell viability. By measuring the absorbance using optical spectroscopy at a wavelength of 570 nm with the Elisa 800 Microplate Reader biotekelx instrument, the percentage of viable cells was determined using a calibration curve with a known number of cells, representing the number of cells on the sample surface. It is noteworthy that comparing the absorbance with the control sample (cells placed in wells without scaffolds) is significant.

2.5.3. Cell adhesion and proliferation

The evaluation of MC3T3 cell interaction with bioactive glass scaffolds was examined through SEM. After the cell incubation period on the samples, fixation was performed. The subsequent step involved dehydrating the samples through incubation in a series of ethanol solutions: 30%, 50%, 70%, 75%, 80%, 85%, 90%, 95%, and 99% EtOH/H_2O, each for 10 minutes. Following dehydration, the samples were dried, and SEM images were captured using a Stereo Scan S360 Cambridge.

3. RESULTS AND DISCUSSION

3.1. Glass Structure and Thermal Behavior

Fig 4 (a) shows the XRD spectra of the glass powders after quenching and grinding. The results confirm the amorphous nature of the bioactive glasses, indicating the successful incorporation of cobalt into the glass structure without the formation of a crystalline phase.

Fig. 4. a) The XRD spectra and b) DTA of bioactive glasses (BGxCo, x= 0, 1, 3, 5)

Fig 4 (b) shows the DTA diagrams for the BG-xCo glass powders after the glass fabricating process. As observed, the glass transition temperature (Tg) generally decreases with increasing cobalt content in the glass, with the most significant decrease observed in the sample containing one percent of cobalt.

However, as the cobalt content is further increased (from 1% to 5%), the Tg value again shows an increase.

The BG-0Co, with 0% Co, displayed a glass transition temperature (Tg) at around 560°C, consistent with the values reported in the literature for similar bioactive glass compositions. For BG-1Co, BG-3Co, and BG-5Co, Tg values of 529, 539, and 545°C, respectively, were determined. Tg increased continuously with increasing Co content in the bioactive glass.

The DTA analysis revealed that cobalt doping influences the glass transition temperatures of bioactive glasses. While a slight amount of cobalt stabilizes the glass matrix, higher doping levels significantly modify the thermal properties. These observations will guide subsequent structural and biological evaluations and may have implications for processing conditions, such as sintering temperatures.

According to the results obtained from thermal analysis and considering the role of cobalt as a glass former in higher percentages (3% and 5%), it leads to an increase in the tendency to crystallization and the appearance of a crystallization peak in glass compositions. It seems cobalt can serve as a nucleating agent in the crystallization process, encouraging the formation of crystalline phases. This is especially useful in controlling the microstructure of the bioactive glass-ceramic after crystallization.

To clarify the impact of cobalt ions on glass structure and their influence on network connectivity, FTIR and Raman spectroscopy were employed.

Fig 5 (a) displays the FTIR survey spectra of the acquired bioactive glass samples. The glass matrix reveals five absorption bands located at approximately 500, 750, 960, 1050, and 1440 cm^{-1}. According to the literature, the bands at around 500 cm^{-1} and ~1050 cm^{-1} can be attributed to Si-O-Si stretching and Si-O-Si bending modes, respectively. The Si-O-Si symmetric stretch observed in pure silica at 450 cm^{-1} is shifted to 500 cm^{-1} in the case of bioactive glasses [14].

The 1440 cm^{-1} peak corresponds to carbonate species adsorbed on the BG surface which can be caused by contamination inside the device. There are no significant differences observed in Co-containing glasses compared to the undoped reference 45S5-modified glass, suggesting that the primary structure of the glass network remains unaltered.

Nevertheless, as the concentration of Co increases in the bioactive glasses, the intensity of the Si-NBO (non-bridging oxygen) peaks at approximately 950 cm^{-1} [15] diminishes and experiences a slight shift towards lower wave numbers. Additionally, the intensity of the Si-O band bending mode at around 750 cm^{-1} decreases with higher cobalt content.

The addition of cobalt to the 45S5-modified base glass (BG1Co sample) increased the intensity of the non-bridging oxygen, (NBO)Si-O peak, observed at approximately 930 cm^{-1}. Moreover, as the cobalt content increases from 1% to 5%, there is a decrease in the intensity of the peak, indicating structural changes in the glass. With an increase in cobalt content from 1% to 5%, there is a reduction in the quantity of non-bridging oxygens, indicating an enhanced connectivity of the glass structure. Therefore, the FTIR analysis suggests that for concentrations ≥3wt% of Co, Co may act as the glass network by forming Si-O-Co bonds, leading to a more highly polymerized SiO_2 network.

The results of Raman spectroscopy for samples containing cobalt are presented in Fig 5 (b). Peaks observed in the 500-800 cm^{-1} range can be attributed to various modes, including bending, symmetric vibrations, and rocking modes of the silicate structure.

Table 2. Glass transition and crystallization temperature of samples

Sample	T_g (ºC)	T_C (ºC)
BG0Co	560	n.a.
BG1Co	529	n.a.
BG3Co	539	850
BG5Co	545	900

6

Fig. 5. a) FTIR spectra and b) Raman spectra of bioactive glasses (BGxCo)

In the higher frequency bands, the peaks can be attributed to symmetric stretching vibrations of Si-O-Si, specifically involving non-bridging oxygen atoms.

According to the literature, the extensive absorption band at approximately ~1100 cm^{-1} is indicative of the asymmetric stretching mode within the Si-O-Si group. Concurrently, the bands located at around ~850 cm^{-1} and ~950 cm^{-1} are linked to Si-O-Si rocking vibrations and the Si-NBO bond, respectively.

The Raman spectroscopy findings demonstrate that diverse bending, vibrational, and stretching states of the tetrahedral units at low frequencies are observable in all samples. The band around ~450 cm^{-1} is likely attributed to defect lines in vitreous silica, a characteristic commonly observed in silicate ring structures [16].

As the cobalt concentrations increase, a distinct reduction in peak intensity is observed for specific vibrational modes within the 500-800 cm^{-1} frequency range. This decrease is attributed to the decrease in the number of bridging oxygens, resulting from reduced network polymerization of the glass.

In the high-frequency range of 800–1200 cm^{-1}, as depicted in Fig 6, peak deconvolution was employed to fit multiple peaks due to the presence of a shoulder and overlapping. The OriginPro software was utilized to analyze this region and identify various structural units within the spectra. Under these conditions, it was assumed that the peaks exhibited a Gaussian distribution. The peaks around 830 cm^{-1}, 930 cm^{-1}, 950 cm^{-1},

1070 cm^{-1}, and 1120 cm^{-1} correspond to the Si–O stretching vibration within the structural units of [SiO$_4$] tetrahedra. The tetrahedral units (Q^n) contain differing quantities of bridging oxygens (n= 0–4), involving stretching vibrations of Q^0 (SiO$_4^{4-}$), Q^1 (Si$_2$O$_7^{6-}$), Q^2 (SiO$_3^{2-}$), Q^3 (Si$_2$O$_5^{2-}$) and Q^4 (SiO$_2$). These units are respectively configured as monomers, dimers, chains, sheets, and three-dimensional networks.

Fig 6 (a) show a column chart illustrating the mole fraction (%) of tetrahedral unit peaks. It is widely recognized that in highly polymerized structures, the contributions of Q^4 and Q^3 units to the glass structure surpass those of the lower-level structural units (Q^0, Q^1, and Q^2) due to the increased presence of bridging oxygens [17, 18].

A contrast between glasses with and without cobalt (Fig 6) indicates a reduction in polymerization in the presence of 1% cobalt. This decrease can be attributed to alterations in the Q^0 and Q^1 units. The conversion of Some parts of the Q^1 unit into the Q^0 unit has led to an increase in the non-bridging oxygen content of the glass structure in specimens containing cobalt. Increasing the cobalt content from 1% to 5% reveals a noticeable decrease in Q^0, accompanied by an observable rise in Q^2 and Q^3 units. This phenomenon is attributed to the higher presence of bridging oxygens. These findings align with the observed reduction in the glass transition of cobalt-containing glasses.

Initially, introducing cobalt into the fundamental glass structure causes a decrease in polymerization, attributed to an elevation in the

ratio of non-bridging to bridging oxygens. Subsequently, there is a notable augmentation in polymerization, characterized by an increase in the ratio of bridging to non-bridging oxygens. The introduction of 1% cobalt to the Base glass induces a structural weakening, leading to a substantial reduction in the glass transition temperature. With an increase in cobalt concentration from 1% to 5%, the structure gains strength, resulting in a higher glass transition temperature for the bioactive glasses. Cobalt's role in bioactive glasses varies with concentration, displaying dual functionality. In the concentration range of 0< x< 3, cobalt functions as a network modifier, shifting to a role as a network former at higher concentrations (≥5%). The impact of incorporating Co into the glass structure and its properties can be analyzed through FTIR and Raman spectroscopy. These findings can be correlated with the thermal behavior of the glass, as determined by DSC measurements. As an intermediate oxide, cobalt can enter into the silicate network, functioning either as a network former or altering the glass structure as a modifier oxide. The observed decrease in the glass transition temperature (T_g) upon the addition of 1% cobalt suggests that cobalt likely enters into the glass network, replacing the Si-O-Si bonds with Si-O-Co bonds.

Consequently, the glass network weakens, leading to a reduction in T_g.

However, the formation of Si-O-Co bonds is more likely at lower cobalt concentrations (≤1%). Hence, it can be concluded that cobalt exhibits a concentration-dependent role in silicate-based bioactive glasses. At weight percentages less than or equal to 1%, it acts as a network former, and at higher percentages (3% and 5%), it can act as a network modifier, replacing Ca^{2+} ions. No significant impact on the structure or thermal behavior was observed through FTIR/Raman spectroscopy and DTA analysis.

As observed, at higher percentages, cobalt can act as a network modifier by replacing Ca^{2+} ions or enter the network and form Si-O-Co bonds as a network former. The lower Tg indicates weaker bonds within the glass network, thereby suggesting an increased potential for enhanced in vitro degradation of the glass scaffolds [19].

3.2. Crystallization and Densification Behavior

To study the crystallization behavior of the glasses, each sample was heat-treated for 30 minutes at its crystallization peak temperature obtained from the DTA. Subsequently, the crystallinity of the samples was analyzed using X-ray diffraction tests.
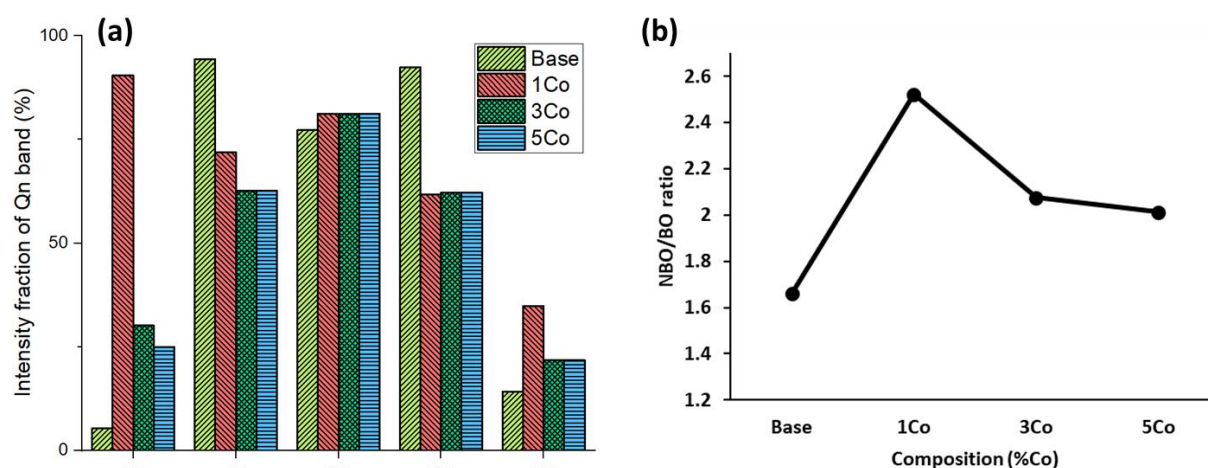

Fig. 6. a) Column chart of the intensity fraction of the tetrahedron unit peaks, b) the non-bridging to bridging oxygens ratio in bioactive glasses with increasing cobalt content

Table 3. The crystallization temperature of bioactive glasses

Sample	T_C (ºC)
BG1Co	n.a.
BG3Co	850
BG5Co	900

For the BG-1Co sample, no crystallization temperature was identified, indicating a lack of tendency for crystallization in these samples. This could be attributed to the more polymerized structure of the bioactive glass (BG-1Co). The crystallization temperature of BG3Co and BG5Co were 850 and 900°C, respectively.

Fig 7 shows the XRD patterns of the specimen heat-treated at the crystallization peak temperatures for 30 min using a heating rate of 10°C/min.
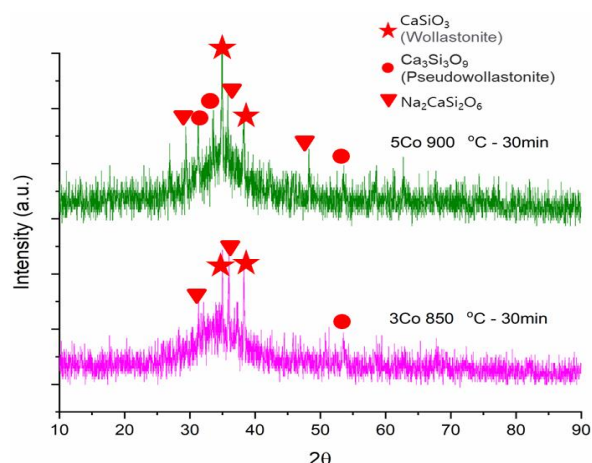
Fig. 7. The X-ray diffraction patterns of the glasses subjected to the one-step heat treatment at the crystallization peak temperatures for 30 min

According to Fig 7, wollastonite ($CaSiO_3$– JCPDS No: 2-0689) and sodium-calcium silicates ($Na CaSi_2O_6$, JCPDS No: 77-2189) have crystallized at the first crystallization peak of each specimen. Additionally, slight peak lines of pseudo wollastonite ($Ca_3Si_3O_9$, JCPDS No: 19-0248) can be detected in the specimen.

The introduction of cobalt into the glass composition causes a slight shift in these crystallization peaks to higher temperatures. Consequently, the increased intensity of crystalline phases could be attributed to the nucleating agent role of cobalt.

The results for the linear shrinkage, water absorption, and apparent shape of samples at different sintering temperatures are presented in Fig 8. Generally, as the sintering temperature increases, water absorption decreases. At the Base sample water absorption is reduced from 1.8% to near 0%. Cobalt contains sample behaviour was the same as the Base sample. Water absorption reduced from about 1.5% to nearly 0% (Fig 8a). It can be said that the water absorption of all

samples is nearly zero, indicating that the water absorption of all samples at temperatures above 700°C was zero. Further examination (Based on appearance) shows that with the increase in temperature to above 700°C, despite the presence of bubbles and closed pores inside the sample, due to the surface of all samples becomes glassy and no water absorption occurs.

In Fig 8 (b), changes in dimensions (expansion) of the samples due to sintering at different temperatures can be seen. The most significant dimensional changes are related to the BG-1Co sample at a sintering temperature of 760°C. Almost all samples sintered at 600°C show a contraction of 20%.

The dimensional changes in samples containing 1 and 3% are similar to each other. With the increase in temperature, the changes first increase sharply, reaching a range of 90-100% (expansion) at 760°C. Afterwards, their dimensional changes decrease, settling in the 40-50% range.

The behavior of the BG-5Co sample at temperatures above 700°C is like that of the Base sample. As the temperature rises, it increases, and after 790°C, it becomes relatively stable at around 20% (expansion). As observed in the appearance of the samples in Fig 8 (d), the dimensional changes in the samples are due to puffing and the foaming effect at temperatures above 700°C.

Examining the appearance of the sample structure at different temperatures in Fig 8 (d) indicates that the size of the formed bubbles (porosity) has increased with temperature. An important note is that the structure of all the bubbles formed as a result of the thermal process is closed. As the sintering temperature has increased, the number of closed pores has decreased, and their size has increased.

Alterations in the bulk density within cobalt-containing samples indicate that the bulk density remains nearly constant as the temperature exceeds 760°C. The crucial observation is that the bulk density in cobalt-containing samples has markedly decreased compared to the Base sample. Furthermore, this difference decreases as the temperature rises. Overall, samples sintered at 650°C exhibit higher density compared to other samples. This observation is relevant for scaffolding design considerations.

To further investigate the effect of cobalt on the microstructure of sintered glass, SEM images of the microstructure of sintered samples at different

temperatures are presented in Fig 9. As seen in Fig 9 (a, b), the glasses sintered at 600 and 650°C are relatively dense. However, with an increase in temperature (≥700°C), a foamy structure is created in the glass. The self-foaming effect during heat treatment and sintering in cobalt-doped bioactive glasses can be attributed to the reduction of Co^{2+} ions to Co^+ ions, which results in the generation of oxygen gas (O_2) and the formation of a porous structure

In recent samples, the size of the pores increases with temperature, reaching 220 μm, 260 μm, 410 μm, and 615 μm at temperatures of 700, 760, 790, and 850°C, respectively (Fig 9).
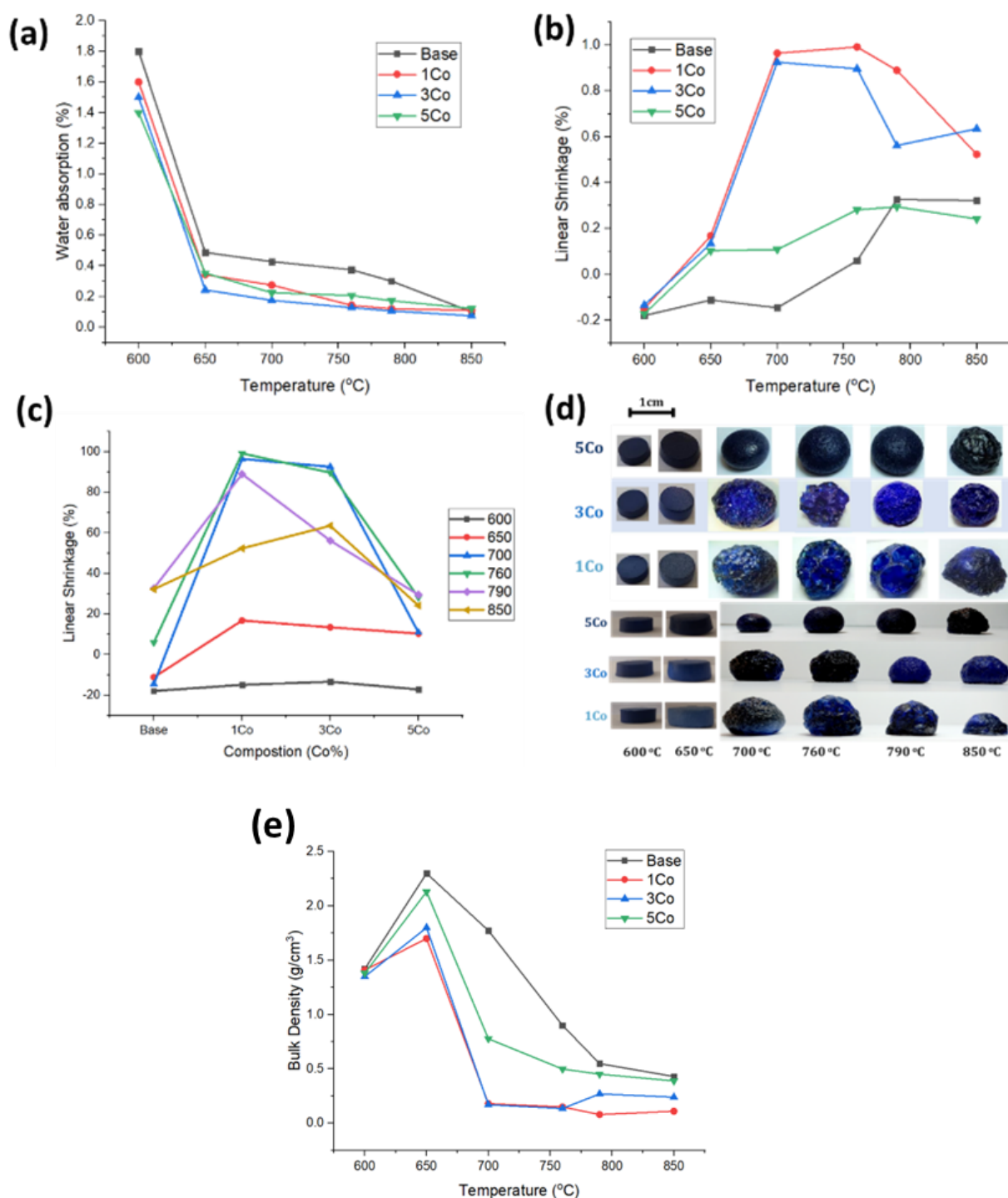
Fig. 8. a) water absorption, b) linear shrinkage in sintering temperature, c) linear shrinkage with cobalt increasing d) apparent shape of bioactive glass samples, e) Changes in bulk density of samples containing cobalt.

Fig. 9. SEM image of the microstructure of samples containing 5% cobalt at temperatures a) 600℃, b) 650℃, c) 700℃, d) 760℃, e) 790℃, and f) 850℃ and microstructure of samples containing g) 1%, h) 3%, and i) 5% cobalt at temperatures 700℃

The microstructures reveal that increasing the percentage of cobalt at a constant temperature reduces the size of the pores in the sample (Fig 9 (g, h, i)). The porosity size of sintered samples at 700°C for 1%, 3%, and 5% cobalt samples was measured as 640 μm, 490 μm, and 220 μm, respectively. The increase in pore size during the sintering process of samples containing cobalt may be attributed to the reactions occurring within the glass structure at temperatures higher than 700°C. The increase in hole size resulting from elevated temperatures may be attributed to heightened chemical reactions, leading to the release of more gases, as well as the reduced surface tension due to the lower viscosity of the glass at higher temperatures [20]. Among the sintered samples containing cobalt, the one sintered at 650°C exhibited a higher density, leading to the selection of this temperature as the appropriate choice for sintering the final scaffolds. The results of XRD phase analysis for the Base samples and BG-5Co sample sintered at the optimal temperature of 650°C are presented in Fig 10. As the results indicate, the level of crystallization in the samples is very low, with almost zero crystallization observed in the Base sample. Crystallization is only present in the samples containing cobalt, highlighting the significant role of cobalt in the crystallization process.

The crystalline phase formed in this glass is wollastonite ($CaSiO_3$), which is consistent with the results obtained in bioactive glasses Based on 45S5. The amount of wollastonite formed in this glass is small.

SEM images of the microstructure of samples are consistent with the results of XRD analysis. As shown in Fig 10 (b,c), the Base sample exhibits a relatively uniform microstructure. In the BG-5Co samples, crystalline phases with rod-like morphology, indicative of the wollastonite phase, are observed.
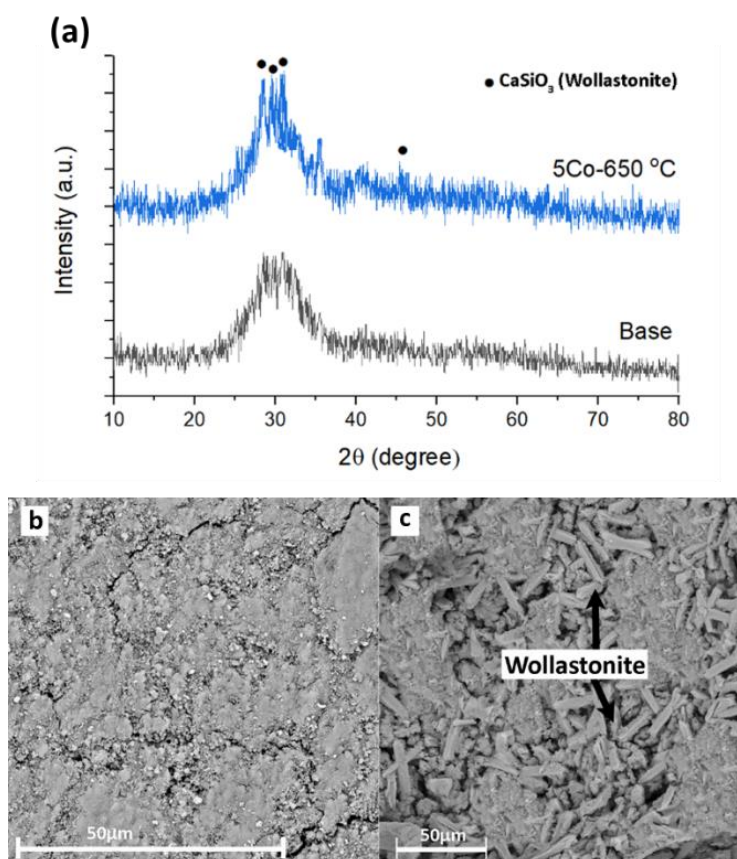
Fig. 10. a) The XRD of Base sample, and BG-5Co fabricated scaffold at 650°C, SEM image of the microstructure of samples sintered at 650°C, b) Base sample, and c) BG-5Co sample

3.3. Scaffold Characterization

3.3.1. Thermal analysis of BG/Resin composite

To determine the appropriate heat treatment schedule for de-binding and subsequent sintering of the scaffolds, the obtained sample underwent a TG test, the results of which can be seen in Fig 11.
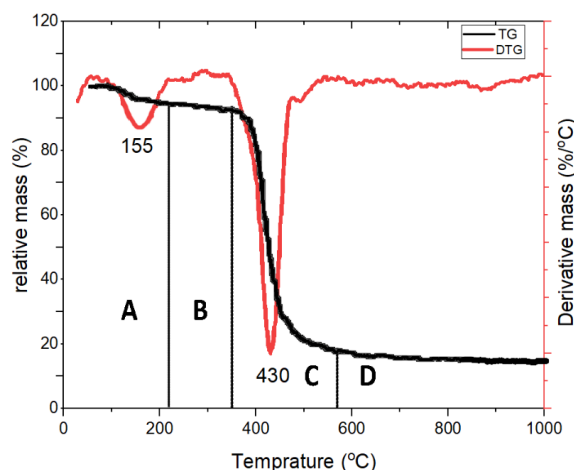
Fig. 11. The TG/DTG analysis of the resin sample

Fig 11 shows the weight loss graph (TG), and its corresponding derivative graph (DTG) for a solid resin sample from 25 to 1000°C. According to the TG curve, the thermal degradation behavior of the polymer phase in the solid resin sample during the de-binding process can be divided into three stages of weight loss. The first stage (Fig 11, part A), from 25 to 227°C, is associated with the loss of physically absorbed water, accounting for approximately 4.53% of weight loss, during which some organic materials, such as acrylate, softened and melted. Afterwards, the weight loss curve plateaus, reaching a constant weight, and the sample's weight remains unchanged (Fig 11, part B). The thermal decomposition of organic components mostly occurs in the third stage (section C) at temperatures ranging from about 350 to 580°C. This stage involves the thermal decomposition of light-sensitive resin, primarily encompassing the decomposition of compounds containing carbon, various aldehyde derivatives, and other macromolecular polyene compounds [21].

The final part of the curve (part D) is associated

12

with the thermal oxidation of residual carbon. The thermal oxidation of residual carbon does not significantly consume heat, and its effect on the thermal analysis process is negligible. As the temperature approaches 1000°C, no obvious weight change is observed in the sample, and the mass change curve remains almost stable. The most significant reduction in resin weight occurs at the peak of the DTG curve, indicating the removal of various organic substances. The de-binding process involves the oxidation and thermal destruction of various components in the resin. Based on the thermal analysis described above, a suitable heat treatment program was designed for sintering the scaffold, as illustrated in Fig 12.

Fig. 12. The heat treatment schedule for resin removal and sintering of scaffolds

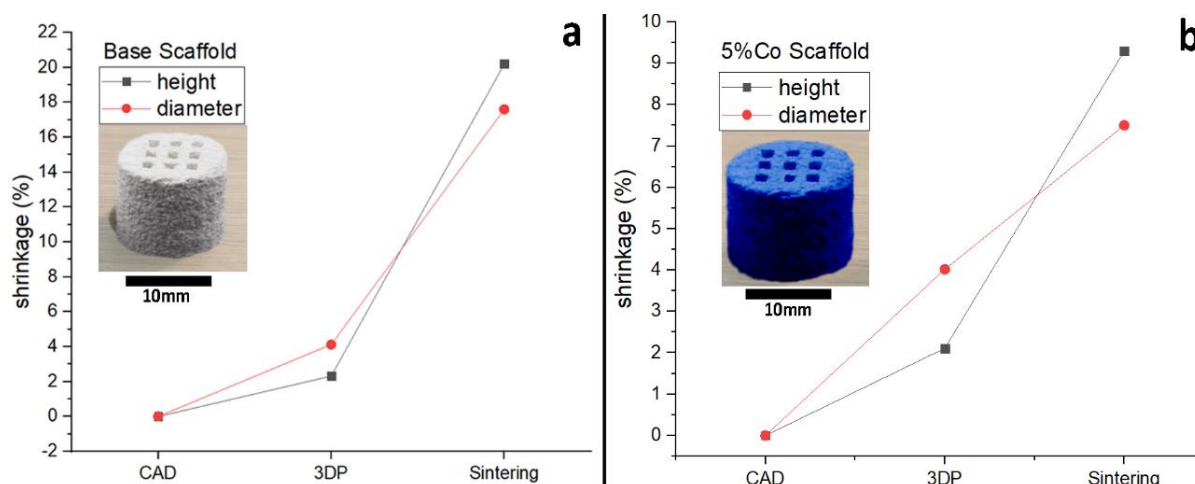### 3.3.2. Post-Treatment and sintering of 3D printed Scaffolds

Fig 13 display images of sintered samples and dimensional changes of scaffolds after design and sintering. As shown, the de-binding and sintering process was executed successfully, resulting in well-sintered scaffolds without any noticeable destructive appearance changes.

As can be seen, scaffolds with interconnected pores with an average size of about 1.5 mm were obtained. Fig 13 shows the amount of shrinkage in the diameter and height of the samples after the sintering process. The Base samples exhibited a height shrinkage of 19% and a diameter shrinkage ranging from 16% to 17%, while in samples containing cobalt, the corresponding values were 9% for height and 7% for diameter.

These results align with the outcomes of the sintering process at 650°C for tablet-shaped samples. In examining the shrinkage of tablet-shaped samples, it was observed that the samples containing cobalt exhibited lower shrinkage compared to both the Base samples and those with 5% copper. Despite variations in shrinkage amounts, all three samples retained their geometric shapes. As evident in the obtained data, a slight anisotropic behavior occurs between the contraction in diameter and the contraction in height according to the designed structure of the scaffold (Fig 13), possibly attributed to the anisotropic design of the sample. Examining the amount of shrinkage in the raw sample (fixed resin) compared to the CAD design reveals that the dimensional changes in all samples are nearly identical. The printed scaffolds are slightly smaller in height and diameter than the CAD designs.

Fig. 13. Diagram of changes in dimensions and appearance of scaffolds a) Base sample, and b) sample containing 5% cobalt.

3.3.3. Characterization of 3Dprinted and sintered bioactive glass scaffolds

The final appearance of the printed samples (Fig 13) shows the proper distribution of the glass powder in the resin field, which has created a uniform structure. In Fig 14, SEM images were taken from the samples to study the microstructure of the printed scaffolds. The SEM images of the sintered Base glass scaffold reveal a well-sintering process, preserving the appearance of the scaffold and its pores. The examination of the microstructure reveals that the sintering process preserved the glass structure effectively. The EDX analysis, taken from different points of the sample (Table 4), indicates the presence of the glassy phase in the Base sample. As seen in the scanning electron microscope images of the microstructure of scaffolds BG-5Co in Fig 14(d) crystallization has occurred in these cobalt-containing samples, unlike the Base scaffold. This difference may be attributed to the longer heat treatment in these scaffolds compared to the Base sinter sample.

EDX analysis reveals that the crystals formed in the sample have a composition close to wollastonite (Table 5), which was also observed in the analysis of sintered samples at 650°C. Wollastonite is a common compound formed during the heat treatment of 45S5-Based glasses [22].

3.4. Bioactivity Assessment

Fig. 14. SEM image of the printed scaffold structure a) raw body before sintering and b, c) Base and d) BG-5Co sintered at 650°C.

Table 4. EDX analysis of the sintered scaffold Base sample

Element	weight percentage (%)	Atomic percentage (%)
O	45.16	60.92
Na	1.21	1.13
Mg	0.59	0.53
Si	36.96	28.53
P	0.81	0.57
K	8.08	4.45
Ca	7.19	3.87

Table 5. EDX analysis from the sintered scaffold sample with the 5% Co composition

Element	crystalline phase		BG-5Co matrix	
	weight percentage (%)	atomic percentage (%)	weight percentage (%)	atomic percentage (%)
O	32.46	49.1	22.86	37.62
Na	3.65	3.85	3.11	3.56
Mg	1.65	1.64	2.84	3.07
Si	21.88	18.85	30.34	28.44
P	10.49	8.2	4.02	3.41
K	3.57	2.44	6.20	4.18
Ca	2.5	1.55	28.74	18.88
Co	0	0	1.89	0.84
Cu	0	0	0	0

3.4.1. *Evaluation of in vitro bioactivity*

The weight and pH changes of the fabricated scaffolds, following immersion in an SBF solution for 1 to 21 days, are shown in Fig 15.

The exchange of cations from the glass Base with hydronium ions in the aqueous solution leads to an increase in the pH values of the solution. The released ions include not only calcium ions but also constituent ions found in the composition of bioactive glass, such as phosphate, magnesium, silica, cobalt, and copper [23]. The release of ions enhances the pH-related indirect antibacterial effect around the sample. In general, the solution's pH changes by about 2 units, indicating the chemical stability of the samples in SBF. The pH values indicate the non-acidic nature of the glass compounds.

As seen in the graph in Fig 15, the pH values of the solution for the Base sample immersed in SBF solution for 21 days increased from 7.4 to 8.8. The pH value increased rapidly on the first day, then gradually increased until the seventh day, and then remained constant during longer immersion times.

This behavior is also observed in the sample containing cobalt, with the pH value remaining constant at 8.6 after reaching this level on the fourth day. However, due to the pH value of $Co(OH)_2$ is lower than that of $Ca(OH)_2$ (Table 6),

the extent of pH changes in the sample containing cobalt is lower than that in the Base sample.

3.4.2. *Hydroxyapatite layer formation on the studied scaffolds*

The formation of CHA was investigated after immersing the Base glass sample in SBF solution for different durations (4 to 21 days). SEM images illustrating the stages of reaction and degradation of scaffolds obtained from the Base bioactive glass are presented in Fig 17.

In the SEM images (Fig 17 (a)) of the scaffold surface after 4 days of immersion in SBF, the formation of a small number of various sediments can be observed. However, analyzing the particles formed on the Base glass scaffold with SEM is challenging due to the superficiality of the reactions. Therefore, complementary analyses using FTIR, XRD, and EDX have been employed to better identify the phases. The results of the EDX analysis in Fig 17 and the XRD analysis in Fig 16 show that the deposits formed on this surface are non-phosphate and non-crystalline compounds, which can be caused by the dissolution of the scaffold itself in the SBF solution. As indicated by EDX analysis, the relative amount of silicon in these compounds is higher than that in the glass, as Ca, P, and Na have dissolved in the solution due to the degradation process.
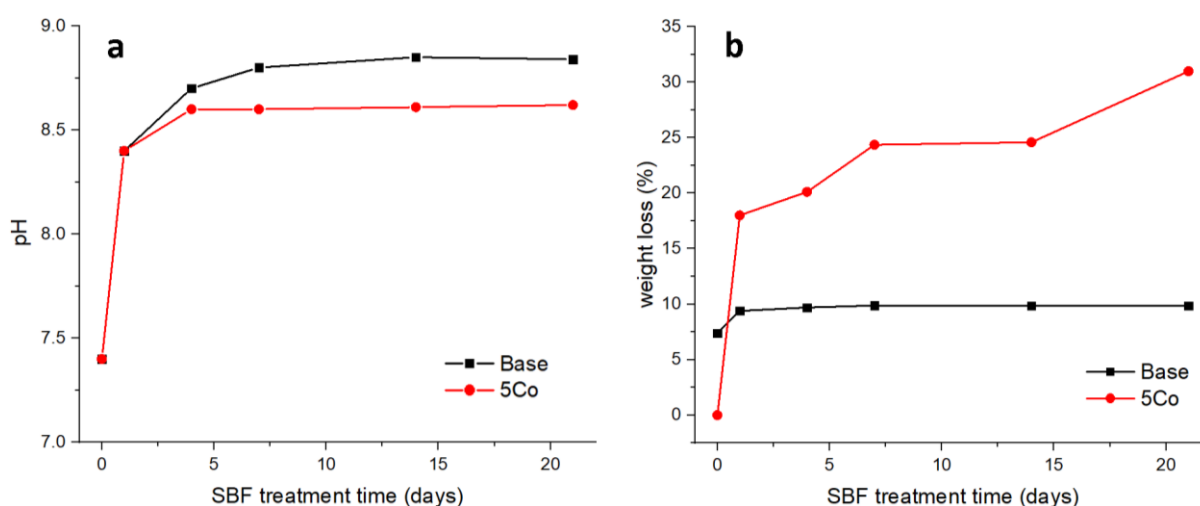
Fig. 15. a) The weight and b) pH changes of the fabricated scaffolds, after immersion in an SBF solution for 1 to 21 days for Base and BG-5Co scaffolds

Table 6. pH value of alkaline solutions of calcium and cobalt compounds

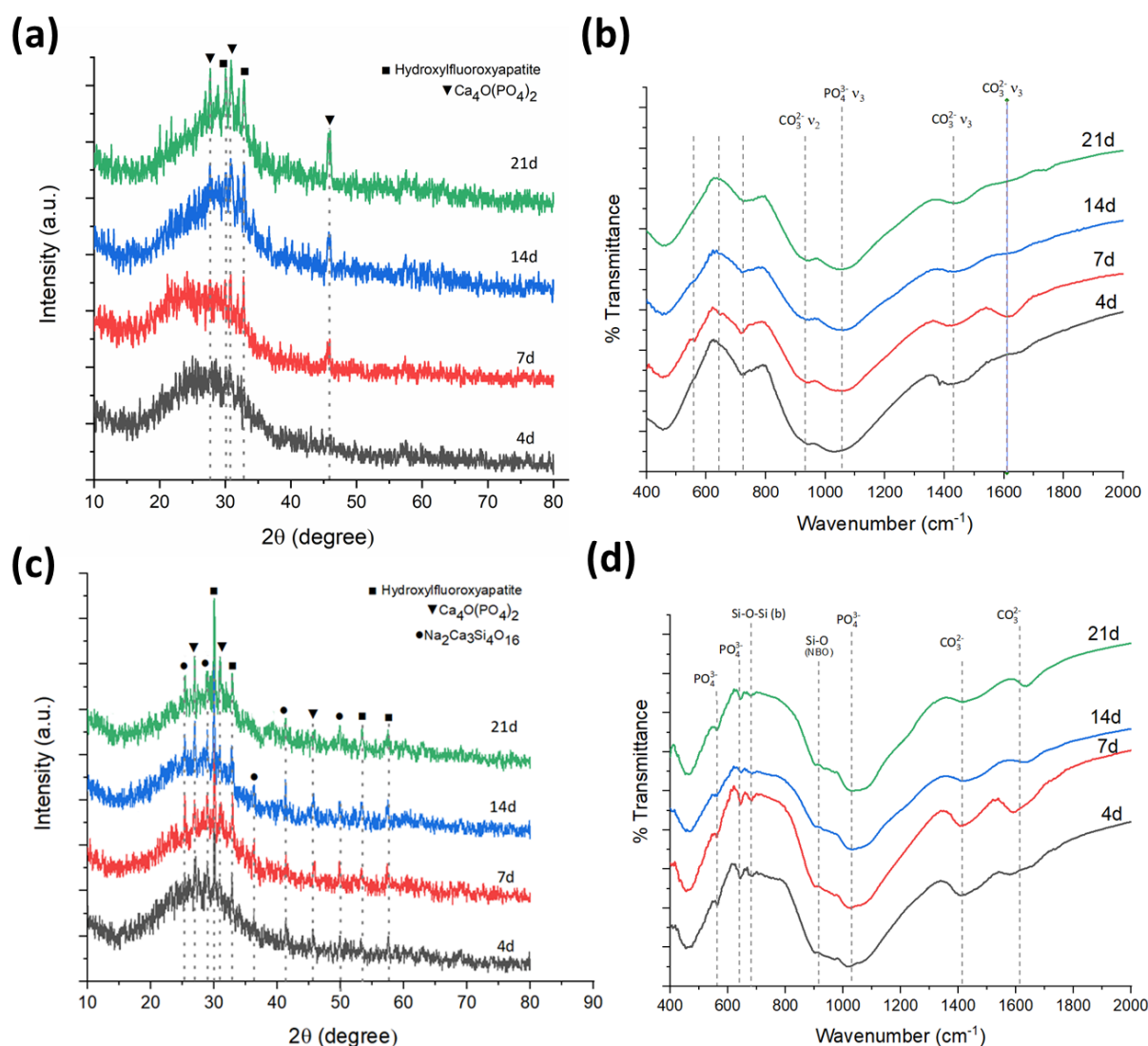| Composition	pH at 1 mM
$Ca(OH)_2$	11.27
$Co(OH)_2$	9.15

15

Based on the SEM images of the surface after 14 days of immersing the scaffold in the SBF solution (Fig 17 (b)), the surface is homogeneously covered with calcium phosphate (CaP) deposits, identifiable by the common morphology of these phases. The results of the EDX analysis in Fig 17 and the XRD analysis in Fig 16 further confirm the formation of calcium phosphate phases.

With an increase in the number of days of immersing the scaffold in SBF solution, the concentration of CaP on the surface of the Base glass scaffold increased and can be observed as small circular particles.

As observed in the XRD results (Fig 16(a)), an increase in the number of days of scaffold immersion in the SBF solution

correlates with heightened peak intensity and, consequently, increased crystallization of calcium phosphate phases. This indicates a rise in the amount of hydroxyapatite formed on the surface.

Fig 16 (b) shows the FTIR spectra of the scaffold with a Base glass composition after immersion for 4, 7, 14, and 21 days in SBF. As observed, the spectrum exhibits peaks at 930, 1428, and 1611 bands, which are associated with the formation of complex carbonate phases preceding the development of hydroxyapatite carbonate. Additionally, the peaks at 560, 630, and 1050 wavelengths can be attributed to the characteristic features of apatite and other phosphate structures, as the P-O bending modes are located in this range [23].

Fig. 16. The sample composition after immersion in SBF for 4-, 7-, 14-, and 21-days a) XRD and b) FTIR for the BG-0Co sample, c) XRD and d) FTIR for BG-5Co

The specific phosphate structure formed in the Base glass composition is the $Ca_4O(PO_4)_2$ phase, as depicted in the XRD results presented in Fig 16, that has a closely apatite structure [24, 25]. Based on the results of various analyses, it can be concluded that the biological activity of the Base scaffolds initiates from the seventh day, and the growth of calcium phosphate phases commences. The results related to the formation of hydroxyapatite (HCA) after 4 to 21 days of immersion in SBF solution were investigated for BG-5Co. The SEM image in Fig 17 (d, e and f) revealed that a continuous and homogeneous silica layer started to grow after 4 days of the samples being immersed in SBF. Simultaneously, calcium phosphate and hydroxyapatite phases began to form in the shape of islands, indicating the high biological activity of the BG-5Co sample.
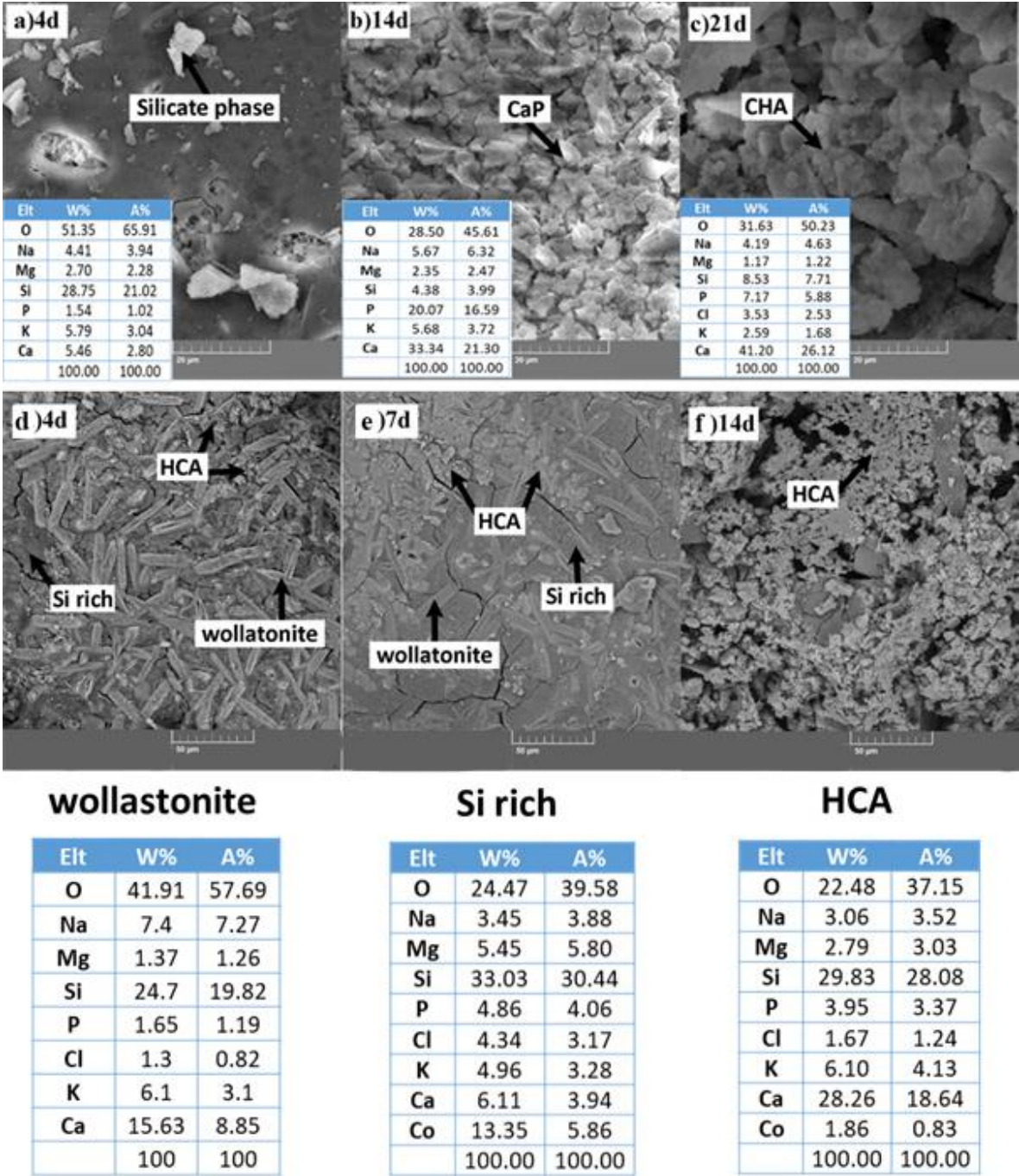

wollastonite

Elt	W%	A%
O	41.91	57.69
Na	7.4	7.27
Mg	1.37	1.26
Si	24.7	19.82
P	1.65	1.19
Cl	1.3	0.82
K	6.1	3.1
Ca	15.63	8.85
	100	100

Si rich

Elt	W%	A%
O	24.47	39.58
Na	3.45	3.88
Mg	5.45	5.80
Si	33.03	30.44
P	4.86	4.06
Cl	4.34	3.17
K	4.96	3.28
Ca	6.11	3.94
Co	13.35	5.86
	100.00	100.00

HCA

Elt	W%	A%
O	22.48	37.15
Na	3.06	3.52
Mg	2.79	3.03
Si	29.83	28.08
P	3.95	3.37
Cl	1.67	1.24
K	6.10	4.13
Ca	28.26	18.64
Co	1.86	0.83
	100.00	100.00

Fig. 17. SEM images of the apatite formation reaction on the surface of the scaffold after immersion in SBF for different periods, a, b and c for BG0Co and d, e and f for BG5Co

This phenomenon may be attributed to the high degradation rate of samples containing cobalt due to their more open structure, as also observed in the results of weight changes. The layer formed on the surface of the sample in the first few days gradually transforms into crystallized phases of hydroxyapatite and calcium phosphate, ultimately reaching their maximum concentration in the sample after 21 days.

A more detailed examination of the process of the formation of different phases due to the placement of the scaffold in the SBF solution over several days reveals the following events occurring at different stages:

After 4 days in SBF solution: The SEM images of the immersed sample after 4 days reveal the formation of a homogeneous and continuous layer surrounding the crystalline phases formed during the sintering process. EDX analysis of the background phase indicates the development of a Si-rich layer between the crystalline phases (Fig 17). Further EDX analysis at other points also demonstrates the crystallization of the hydroxyapatite phase (HCA) and amorphous calcium phosphate (Cap) phases.

In the phases developed within the samples by the fourth day, cobalt elements are observable in the Si-rich mixed layer. Intriguingly, cobalt penetrates the Si-rich layer, indicating the diffusion of cobalt ions through the SiO_2 layer.

Additionally, traces of cobalt ions are evident in the composition of calcium phosphate. Altering the chemical composition of the CaP layer appears to influence cellular response. The inclusion of cobalt in calcium phosphates enhances osteoclast proliferation and overall mineral reabsorption. Consequently, in the initial days, the formation of the hydroxyapatite phase is observed in this sample (Fig 17). In the SEM images depicted in Fig 17, a silica-rich layer, upon which calcium phosphate-like phases have commenced crystallization, envelops the sample's surface. The P-O peaks, arising from the crystallization of these phases, are observable as a broad peak within the 1060 cm^{-1} range and as narrow peaks spanning the 550 to 650 cm^{-1} range (Fig 16(d)).

The formation of carbonate hydroxyapatite can be identified by the emergence of triplets in the bending modes (ν3) associated with the O-P-O bands of CHA at 550 and 1650 cm^{-1}. The peaks at the wavelengths of 1430 cm^{-1} and 1161 cm^{-1} can be attributed to V3(CO_3^{2-}) present in carbonate ions formed because of CHA crystallization. The initiation of crystallization for these phases can be observed in the XRD analysis at 2θ angles of approximately 27, 29, 31, 33, 46, 53, and 58 degrees. The results of the XRD analysis indicate that the crystallization of calcium phosphate and hydroxyapatite phases commenced from the very first days (Fig 16(c)).

The results of XRD analysis of the samples throughout all days indicate that the wollastonite phase has remained stable during the degradation process. Crystallization in the scaffolds produced by the 3D printing method is greater than in the samples manufactured by the press method, as the crystalline phases have had the opportunity to nucleate and grow during the extended sintering process.

After 7 Days in SBF: The SEM images in (Fig 17) show that as the immersion time of the scaffolds in the SBF solution increases, the silicate layer grows more, surrounding the crystalline phases. Additionally, the amount of calcium phosphate phases in the 7-day sample increases, indicating a rise in the formation of phosphate and hydroxyapatite phases.

The results of FTIR analysis in Fig 16 show that the intensity of the double bands at 1560 cm^{-1} and 1650 cm^{-1}, which are related to the vibrational modes of PO_4^{3-} groups, has increased. Additionally, the intensity of the double peaks at the wavelengths of 1430 cm^{-1} and 1160 cm^{-1}, corresponding to (CO_3^{2-}) in the carbonate ions formed by the crystallization of HCA, has slightly increased.

The XRD analysis of the 7-day sample indicates an increase in the intensity of calcium phosphate ($Ca_4O(PO_4)_2$) and hydroxyapatite phases. These phases correspond to the peaks observed in the 560 to 1650 cm^{-1} wavelengths of the FTIR spectrum.

After 14 days in SBF solution: The SEM images of Fig 17 taken on the 14th day show a significant increase in the amount of hydroxyapatite crystalline phase, covering almost the entire surface of the sample. The formation of hydroxyapatite can be attributed to the increased intensity of calcium phosphate bands (double bands from 1560 cm^{-1} to 1650 cm^{-1}) in FTIR. Additionally, the intensity of the double peaks at the wavelengths of 1430 cm^{-1} and 1603 cm^{-1} has decreased, indicating the potential transformation

of carbonate phases into the natural carbonate hydroxyapatite (CHA) phase. The XRD analysis of the 14-day sample reveals a greater growth of the hydroxyapatite phase compared to the calcium phosphate phase ($Ca_4O(PO_4)_2$). This suggests the conversion of intermediate phases of calcium phosphate to hydroxyapatite, consistent with the results related to the phase wavelengths of calcium phosphate observed in FTIR.

After 21 days in SBF solution: The intensity of calcium phosphate bands (double bands from 1560 cm⁻¹ to 1650 cm⁻¹) has increased, and the intensity of the double peaks at the wavelengths of 1430 cm⁻¹ and 1150 cm⁻¹ has decreased. This change can be attributed to the conversion of carbonate phases into Natural hydroxyapatite carbonate (HCA). The XRD analysis of the 21-day sample reveals an increased growth of the calcium phosphate phase ($Ca_4O(PO_4)_2$) and the hydroxyapatite phase. Consequently, the intensity of the peak related to the crystallization of these two phases has increased. Upon examining and comparing the two Base samples with the BG-5Co sample, it is evident that the presence of cobalt has accelerated the formation of calcium phosphate and hydroxyapatite. Although the formation of calcium phosphate phases commenced on the 4th day in both samples, the sample containing cobalt also initiated the formation of the hydroxyapatite phase. Considering the time point at which the calcium phosphate layers begin and the formation of the hydroxyapatite phase as indicators of the bioactivity of glasses, we can conclude that the bioactivity of scaffolds has increased under the influence of cobalt.

Based on the results obtained from SEM, EDX, XRD, and FTIR analyses, we can consider the following points regarding the physical-chemical reactions of cobalt-containing scaffolds.

The mechanism of apatite formation on BG-5Co scaffolds can be described as follows:

Immersion in SBF after 1 to 4 days: Based on the results obtained, it can be asserted that the occurrences in the cobalt-containing sample align with those in the Base samples, differing only in the kinetics of the process. Consequently, all the events unfold within the first four days.

The initial reaction of the bioactive glass (BG) surface and the release of Na^+, Ca^{2+}, and Co^{2+} around the scaffold occur in an ion exchange reaction with H^+ from the SBF solution, according to the following equation (Eq. 1):
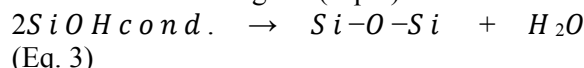
$$Si-O-Na^+ + H_2O \rightarrow Si-OH + OH^- + Na^+$$
(Eq. 1)

Soluble Si species are released in the glass surface area as soon as the Si-O bonds are broken by hydrolysis (Eq. 2):

$$Si-O-Si + H_2O \rightarrow Si-OH + HO-Si$$
(Eq. 2)
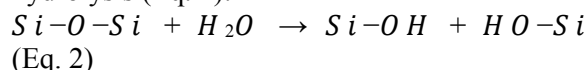
The formation of silanols is activated by both above-mentioned reactions. SiO_2 phases are formed by condensation of SiOH groups on the surface of bioactive glass (Eq. 3):

$$2SiOH\,cond. \rightarrow Si-O-Si + H_2O$$
(Eq. 3)

FTIR analysis can confirm the presence of these specific areas. Based on this data, one can assume that, after 4 days of immersion, a mixed phase of CaP+ Si_xO_y forms on the surface of the scaffolds, replacing the specific ACP layer on the silica gel as proposed by Hank et al. In samples containing cobalt, this mixed phase also incorporates cobalt ions.

The presence of cobalt ions in these phases from the early hours of their formation intensifies the crystallization process, absorbs more mineral elements, and accelerates the crystallization of the hydroxyapatite phase. The analyses confirmed the enhanced apatite formation ability of the cobalt-containing scaffolds after 4 days of immersion in SBF. Despite some reports in articles about the potential negative effect of crystallinity on the bioactivity of bioactive (sintered) glass scaffolds, this study observed high bioactivity comparable to that of amorphous bioactive glass products reported in the literature.

Furthermore, the rapid formation of CHA in micron particles of bioactive glass 45S5 was observed after a 4-day immersion in SBF. Additionally, it was confirmed that the presence of cobalt in 45S5 bioactive glass not only has no negative effect on the ability to form CHA but also accelerates the crystallization process of calcium phosphate phases and, consequently, hydroxyapatite.

3.5. Stability and Cytotoxicity of Sintered Scaffolds

3.5.1. *cytotoxicity (MTT)*

The effect of the scaffold composition on cell proliferation was measured using the MTT method. The test results are given as a percentage of live cells compared to the control sample in Fig

18. This test was performed Based on evaluating the viability of MC3T3 cells in 3 days and 7 days. Examining cell toxicity and cell culture in laboratory conditions, it has been observed that the Base sample is completely non-toxic in the cell culture environment, but the toxicity of samples containing cobalt changes over time.

Fig. 18. Viability of cells (%) revealed by MTT for all samples (BG-xCo)

As can be seen in the results, with the addition of cobalt to the samples, the level of toxicity increases. This process was observed both on the 3 day and the 7th day. The noteworthy point is that the toxicity levels of both samples are dependent on time and have increased over time. The reason for the increase in toxicity could be due to the increase in the release of cobalt into the environment, which was also observed in the decay data.

3.5.2. Cell adhesion

To further investigate the interaction between cells and the surface of bioactive glasses, pictures were taken of the surface of the samples. Fig 19 shows the scanning electron microscope images of the morphology of spread MC3T3 cells and how the cells are attached to the surface. As can be seen in the figure, MC3T3 cells are well spread on the surface of the Base samples and the cell can be well spread on the rough surfaces of the printed scaffolds by bridging. The results obtained for the Base sample on days 3 and 7 are the same, and the adhesion and spreading are well done. Fig 19 related to the surface of the Base scaffolds, Base and cobalt-containing samples in the analysis of cell adhesion and stability. The results obtained in the scanning electron microscope images are consistent with the

toxicity results. The rate of cell growth in the sample containing cobalt has decreased from 3 days to 7 days, and this is a sign of the toxicity of the scaffold and the lack of survival of the cells over time. However, the noteworthy point is that the 3-day samples have very good adhesion and as can be seen, the cells have been able to spread on the surface of the scaffold with different mechanisms such as bridging.

4. CONCLUSION

This study investigates the role of cobalt in altering the properties and bioactivity of 45S5 bioactive glass. Cobalt's integration shows a dual impact: at low levels it disrupts the network, lowering the glass transition temperature (Tg), while at higher concentrations it enhances polymerization and structural strength. Crucial to understanding these changes, XRD confirms the amorphous character of the glasses, indicating a successful fusion of cobalt into their structure.

DTA reveals a non-linear relationship between cobalt content and Tg, suggesting a concentration-dependent impact. Spectroscopic analysis with FTIR and Raman further reveals how cobalt affects the glass network, with higher concentrations potentially inducing Si-O-Co bond formation and influencing SiO_2 polymerization.

The study uncovers the nucleating role of cobalt, fostering crystalline phases within glass ceramics, beneficial for certain applications. Rapid CHA layer formation in SBF due to cobalt demonstrates substantial bioactivity, essential for biomedical material integration. Contrary to previous assumptions, crystallinity from cobalt-induced calcium phosphate phases does not impede bioactivity but rather bolsters scaffold mineralization, vital for bone tissue engineering.

In summary, cobalt-doped bioactive glass scaffolds emerge as highly bioactive materials with adjustable thermal and structural characteristics suitable for regenerative medicine, showcasing the versatility and potential for improved tissue integration and healing.

REFERENCES

[1]. Lee SS, Du X, Kim I, Ferguson SJ. "Scaffolds for bone tissue engineering". Matter. 2022, 9, 2722-59.

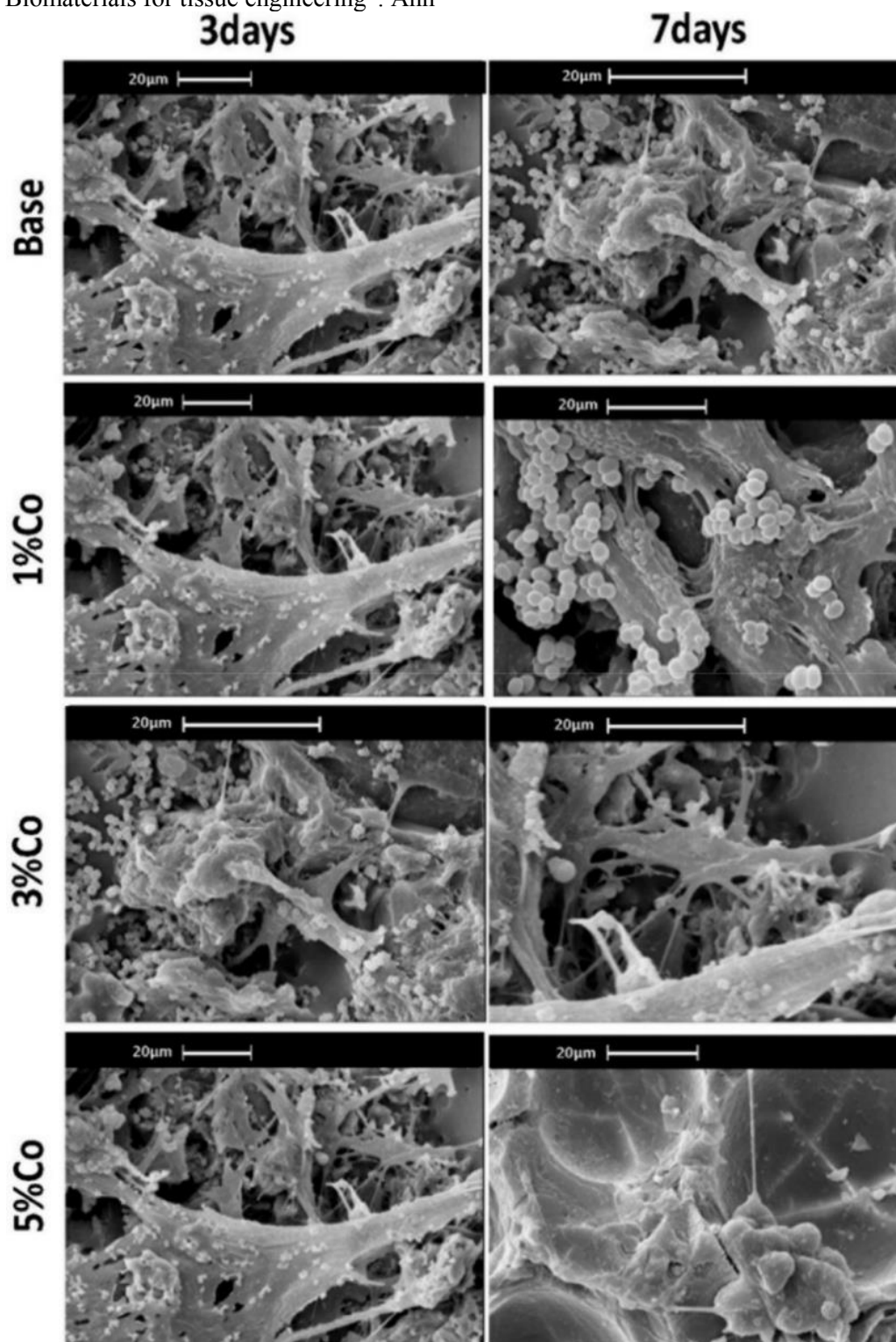[2]. Lee EJ, Kasper FK, Mikos AG. "Biomaterials for tissue engineering". Ann Biomed Eng. 2014, 42, 323–37.

3days **7days**

Fig. 19. Results of cell attachment study after 3 and 7 days for BG-xCo samples

[3]. Sharma S, Sudhakara P, Singh J, Ilyas RA, Asyraf MRM, Razman MR. "Critical review of biodegradable and bioactive polymer composites for bone tissue engineering and drug delivery applications". Polymers (Basel). 2021, 13,

21

2623.

[4]. Fiume E, Barberi J, Verné E, Baino F. "Bioactive glasses: from parent 45S5 composition to scaffold-assisted tissue-healing therapies". J Funct Biomater. 2018, 9(1), 24.

[5]. Kermani F, Vojdani-Saghir A, Beidokhti SM, Nazarnezhad S, Mollaei Z, Hamzehlou S, et al. "Iron (Fe)-doped mesoporous 45S5 bioactive glasses: Implications for cancer therapy". Transl Oncol. 2022, 20, 101397.

[6]. Arango-Ospina M, Boccaccini AR. "Bioactive glasses and ceramics for tissue engineering". Tissue engineering using ceramics and polymers. Elsevier, 2022, 111–78.

[7]. Nicholson JW. "Periodontal Therapy using Bioactive glasses: a review". Prosthesis. 2022, 4(4), 648–63.

[8]. Fiume E, Migneco C, Kargozar S, Verné E, Baino F. "Processing of bioactive glass scaffolds for bone tissue engineering". Bioactive Glasses and Glass-Ceramics: Fundamentals and Applications. 2022, 119–45.

[9]. Salazar DAA, Fedin M, Hartramph W, Brauer DS. "The structural role and coordination environment of cobalt in $45P_2O_5$–CaO–Na_2O phosphate glasses: thermal properties and Raman, UV–vis-NIR, and EPR spectroscopy". Dalton Transactions. 2023, 52(14), 4526–36.

[10]. Littmann E, Autefage H, Solanki AK, Kallepitis C, Jones JR, Alini M, et al. "Cobalt-containing bioactive glasses reduce human mesenchymal stem cell chondrogenic differentiation despite HIF-1α stabilization". J Eur Ceram Soc. 2018, 38(3), 877–86.

[11]. Baino F, Montazerian M, Verné E. "Cobalt-Doped Bioactive Glasses for Biomedical Applications: A Review". Materials. 2023, 16(14), 4994.

[12]. Gavinho SR, Graça MPF, Prezas PR, Kumar JS, Melo BMG, Sales AJM, et al. "Structural, thermal, morphological and dielectric investigations on 45S5 glass and glass-ceramics". J Non Cryst Solids. 2021, 562, 120780.

[13]. Kokubo T, Kushitani H, Sakka S, Kitsugi T, Yamamuro T. "Solutions able to reproduce in vivo surface-structure changes in bioactive glass-ceramic A-W3". J Biomed Mater Res. 1990, 24(6), 721–34.

[14]. Jaimes AT, Kirste G, de Pablos-Martín A, Selle S, de Souza e Silva JM, Massera J, Karpukhina N, Hill RG, Brauer DS. "Nano-imaging confirms improved apatite precipitation for high phosphate/silicate ratio bioactive glasses". Scientific reports. 2021, 30, 11(1), 19464.

[15]. Kiran. P, Ramakrishna. V, Udayashankar. N.K., Shashikala. H.D, "The effective role of alkali earth/alkali ratio on formation HCA nano particles for soda lime phosphor silicate glass system". OpenNano, 2017, 2, 47-56.

[16]. Özarslan AC, Yücel S. "Comprehensive assessment of SrO and CuO co-incorporated 50S6P amorphous silicate bioactive glasses in vitro: Revealing bioactivity properties of bone graft biomaterial for bone tissue engineering applications". Ceramics International. 2023, 49(9), 13940-52.

[17]. Pedone A, Cannillo V, Menziani MC. "Toward the understanding of crystallization, mechanical properties and reactivity of multicomponent bioactive glasses". Acta Mater. 2021, 213, 116977.

[18]. Prasad S, Gaddam A, Jana A, Kant S, Sinha PK, Tripathy S, et al. "Structure and stability of high CaO-and P_2O_5-containing silicate and borosilicate bioactive glasses". J Phys Chem B. 2019, 123(35), 7558–69.

[19]. Fábián M, Kovács Z, Lábár JL, Sulyok A, Horváth ZE, Székács I, et al. "Network structure and thermal properties of bioactive (SiO_2–CaO–Na_2O–P_2O_5) glasses". J Mater Sci. 2020, 55(6), 2303–20.

[20]. Erasmus EP, Sule R, Johnson OT, Massera J, Sigalas I. "In vitro evaluation of porous borosilicate, borophosphate and phosphate bioactive glasses scaffolds fabricated using foaming agent for bone regeneration". Sci Rep. 2018, 8(1), 3699.

[21]. Wojnowski W, Kalinowska K, Majchrzak T, Zabiegała B. "Real-time monitoring of the emission of volatile organic compounds from polylactide 3D printing filaments". Science of the Total Environment. 2022, 805, 150181.

[22]. Fernandes HR, Gaddam A, Rebelo A, Brazete D, Stan GE, Ferreira JMF. "Bioactive glasses and glass-ceramics for healthcare applications in bone regeneration and tissue engineering". Materials. 2018, 11(12), 2530.

[23]. N. Yazdani, J. Javadpour, B. Eftekhari Yekta and M. Hamrang, "Hydrothermal Synthesis of Cobalt- Doped Hydroxyapatite Nanoparticles: Structure, Magnetic Behaviour, Bioactivity and Antibacterial Activity", Iranian Journal of Materials Science & Engineering, 2019, 16(1), 39-48. DOI: 10.22068/ijmse.16.1.39

[24]. Mecca FG, Bellucci D, Cannillo V. "Effect of thermal treatments and ion substitution on sintering and crystallization of bioactive glasses: A review. Materials". 2023 Jun 28, 16(13), 4651.

[25]. Lu X, Kolzow J, Chen RR, Du J. "Effect of solution condition on hydroxyapatite formation in evaluating bioactivity of B_2O_3 containing 45S5 bioactive glasses". Bioactive materials. 2019, 4, 207-14.

23